1 # Influence of Fe(II), Fe(III) and Al(III) Isomorphic Substitutions on

2 # Acid-Base Properties of Edge Surfaces of Cis-Vacant

3 # Montmorillonite: Insights from First-Principles Molecular Dynamics

4 # Simulations and Surface Complexation Modeling

5 **Revision 1**

6 **Pengyuan Gao[1,2,3], Xiandong Liu[4,5], Zhijun Guo[1,2], Christophe Tournassat[3,6*]**

7

8 *1. Radiochemistry Laboratory, School of Nuclear Science and Technology, Lanzhou University,*
9 *Lanzhou 730000, China*
10 *2. Frontiers Science Center for Rare Isotopes, Lanzhou University, Lanzhou 730000, China*
11 *3. Institut des Sciences de la Terre d'Orléans, Université d'Orléans-CNRS-BRGM, Orléans 45071,*
12 *France*
13 *4. State Key Laboratory for Mineral Deposits Research, School of Earth Sciences and*
14 *Engineering, Nanjing University, Nanjing 210093, China*
15 *5. Frontiers Science Center for Critical Earth Material Cycling, Nanjing University, Nanjing*
16 *210023, China*
17 *6. Earth and Environmental Sciences Area, Lawrence Berkeley National Laboratory, Berkeley,*
18 *California 94720, USA*

19

20 *** Corresponding author: <u>christophe.tournassat@univ-orleans.fr</u>**
21
22
23

24 **Abstract**

25   Knowing the influence of isomorphic substitutions on the acid-base properties of

26 smectite edge surfaces is an important aspect of the detailed understanding of clay

27 minerals' interfacial properties with implications in the modeling of adsorption

28 processes. We investigated the intrinsic acidity constants of Fe(II)/Fe(III) and Al(III)

29 substituted edge surface sites of montmorillonite with a cis-vacant structure, which

30 includes four crystallographic orientations perpendicular to [010], [0$\bar{1}$0], [110] and

31 [$\bar{1}$$\bar{1}$0], using the FPMD (first-principles molecular dynamics) based vertical energy

32 gap method. Fe(II) and Fe(III) substitutions resulted respectively in a significant

33 increase and decrease in pKa values at amphoteric groups directly associated with Fe

34 octahedra. In addition, Fe(II) substitution increased the pKa values of the neighboring

35 silanol sites, while Fe(III) substitution had a weak influence on these sites. The

36 Al-substituted tetrahedra had amphoteric sites with higher pKa values than the

37 non-substituted Si tetrahedra, and they increased significantly the pKa values of the

38 sites bridging the tetrahedral and octahedral sheets on surfaces perpendicular to [010]

39 and [110]. The acid-base properties of substituted and non-substituted surface sites of

40 cis-vacant montmorillonite were used to build a state-of-the-art surface complexation

41 model, which successfully reproduced the best available experimental acid-base

42 titration data. This model was further used to predict acid-base properties of

43 dioctahedral smectites (montmorillonite, beidellite, and nontronite) according to their

44 cis- or trans-vacant structures and their layer chemistry. According to these

45 predictions, these smectites exhibit very similar overall pH buffering properties,

46   despite significant differences in structure and chemistry. A detailed analysis of the

47   acid-base properties as a function of crystallographic directions evidenced, however,

48   that these differences should have a large influence on the adsorption properties

49   towards ionic species.

50   **Keywords:** first-principles molecular dynamics, surface complexation modeling, clay,

51   cis-vacant, trans-vacant, montmorillonite, Fe(II)/Fe(III) isomorphic substitution,

52   Al(III) isomorphic substitution, pKa

53   **INTRODUCTION**

54   2:1 type clay minerals are characterized by layered structural units consisting of

55   two tetrahedral silica sheets sandwiching one octahedral aluminum sheet (TOT,

56   Tetrahedron-Octahedron-Tetrahedron) (Tournassat et al. 2015). Octahedra bear two

57   OH groups that are in adjacent or opposite positions in cis- and trans-octahedra

58   respectively. In dioctahedral clay mineral layers, a third of the octahedra are vacant,

59   and, depending on the vacancy position, TOT layers are thus described with either

60   trans- or cis-vacant structures, which are respectively centrosymmetric or not

61   (Tsipursky and Drits 1984; Brigatti et al. 2011; Gao et al. 2023). Montmorillonites,

62   which are part of the most studied clay minerals, have most commonly a cis-vacant

63   structure, such as, for example, reference Wyoming and Kunipia montmorillonite

64   (Subramanian et al. 2020; Orucoglu et al. 2022). Heterovalent structural isomorphic

65   substitutions of cations in cis-vacant TOT layers create a permanent negative layer

66   charge (Brigatti et al. 2006) (Fig. 1). Iron occurs in clay minerals in both Fe(II) and

67   Fe(III) oxidation states and it can participate in redox reactions and influence the

68   surface properties of clay minerals as well as the adsorption process (Stucki 2013).

69   Fe(II) and Fe(III) mainly exist in the octahedral sheet while minor quantities of Fe(III)

70   can substitute for Si(IV) in the tetrahedral sheet (Brigatti et al. 2006; Kéri et al. 2017).

71   Kéri et al. proposed that there is no preferential occupation of cis- or trans-octahedra

72   by Fe(II) and Fe(III) in low Fe-bearing bulk montmorillonite (Kéri et al. 2017),

73   consistent with that of Mg(II) substitution in the octahedral sheet (Drits and Zviagina

74   2009). Moreover, the common isomorphic substitutions in the tetrahedral sheet are

75   Al(III) for Si(IV) tetrahedral (Brigatti et al. 2006). The influence of isomorphic

76   substitutions on smectite properties has received extensive attention because it affects

77   many physical-chemical properties, such as its ability to adsorb and exchange other

78   ions (Liu et al. 2022). The substitution effect can also influence the clay density,

79   porosity, and surface area, as well as its reactivity and stability (Bergaya et al. 2006).

80   Therefore, a thorough understanding of the substitution effects involved is essential

81   for elucidating the natural properties of clays.

82   Clay minerals' surfaces exhibit adsorptive properties affecting the fixation and

83   migration of metals, metalloids, and organics in natural and engineered environments

84   (Tournassat et al. 2015; Sposito et al. 1999; Bergaya and Lagaly 2006; Kome et al.

85   2019). Understanding the interfacial reactivity of clay minerals can help researchers

86   and environmental engineers develop effective strategies for managing the

87   contamination of soil and water by metal ions and other pollutants, using surface

88   complexation models (SCMs) to predict contaminant adsorption and mobility in

89   clay-rich environments as a function of chemical solution conditions in time and

90   space (Tournassat et al. 2018).

91   TOT layers exhibit two kinds of surfaces, i.e. basal and edge surfaces. Structural

92   layer negative charge originating from isomorphic substitutions leads to the property

93   of cation exchange at basal surfaces, while high chemical reactivity occurs at the edge

94   surfaces (Liu et al. 2022). Acidity (pKa) of edge surfaces is a key property related to

95   other interfacial chemical reaction properties, such as adsorption or surface nucleation

96   (Davis et al. 1978; Lagaly 2006; Mccabe and Adams 2013). Substitutions can affect

97   the acidity of edge surface sites because they alter the electronic structure of the clay,

98   which thus affects the surface acid-base properties (Schoonheydt and Johnston 2006;

99   Liu et al. 2014a, 2015a). Structural formulas of two reference clay mineral samples,

100   Swy-2   and   MX80   montmorillonites,   are   respectively

101     $(S_{i3.87}Al_{0.13})(Al_{1.52}Mg_{0.25}Fe_{III0.224}Fe_{II0.006})Na_{0.39}O_{10}(OH)_2$ and

102     $(Si_4)(Al_{1.57}Mg_{0.25}Fe^{III}_{0.09}\text{-}Fe^{II}_{0.09})Na_{0.34}O_{10}(OH)_2$ (Duc et al. 2005b). Ideally, the

103   chemical complexity of the structural formula of clay layers should be taken into

104   account to build predictive SCMs based on thermodynamic equilibrium equations

105   (Gao et al. 2023; Bourg et al. 2007; Tournassat et al. 2016). An accurate SCM requires

106   knowledge of the influence of various isomorphic substitutions on the acidity value of

107   the edge surface sites.

108   A common experimental method for investigating the acid-base reactivity of clay

109   minerals is acid-base titration (Duc et al. 2005b; Bourg et al. 2007; Baeyens and

110   Bradbury 1997; Charlet et al. 1993; Duc et al. 2005a, 2008, 2006; Tombácz and

111   Szekeres 2004, 2006; Wanner et al. 1994; Zysset and Schindler 1996). In 2016,

112   Tournassat et al pooled available pKa values derived from ab initio calculations based

113   on a trans-vacant model into SCMs to yield reasonable prediction of the titration data

114   of montmorillonite edge surfaces (Tournassat et al. 2016). However, the modeled

115   edge-specific surface area did not fully agree with the experimentally measured

116   values, which may be ascribed to the fact that the titration data were obtained on

117   montmorillonite samples with a cis-vacant structure (Tournassat et al. 2016).

118   Cis-vacant structures are not centrosymmetric, which indicates that the edges

119   perpendicular to the [010] and [0$\bar{1}$0], [110] and [$\bar{1}\bar{1}$0] are different (Tsipursky and

120   Drits 1984). In a previous study, we showed that cis-vacant and trans-vacant model

121   edge surfaces have similar average charge behaviors for edges perpendicular to the

122   [010] and [0$\bar{1}$0] crystallographic directions, but distinct average charge behaviors for

123   [110] and [$\bar{1}\bar{1}$0] crystallographic directions (Gao et al. 2023). Although our previous

124   study pointed out the lack of constraints from potentiometric titration data for SCMs,

125   whether this difference is effective for further improving the fit of the acid-base

126   titration data remained to be investigated. Currently, pKa values of non-substituted

127   and Mg(II)-substituted layers of cis-vacant montmorillonite have been evaluated (Gao

128   et al. 2023), and a key to the above-mentioned problem may be related to a lack of

129   availability of a complete set of acidity constants for cis-vacant montmorillonites. The

130   influence of Fe(II)/Fe(III) and Al(III) isomorphic substitutions on the pKa values at

131   montmorillonite edge surface sites thus remained to be determined.

132   First-principles molecular dynamics (FPMD) has been recognized as a powerful

133   tool in the field of interfacial geochemistry (Leung et al. 2009; Leung and Criscenti

134 2012). By combining FPMD and the vertical energy gap method, the interfacial

135 intrinsic pKa values can be reliably estimated (Cheng and Sprik 2010; Sulpizi et al.

136 2012; Tazi et al. 2012; Liu et al. 2013b, 2013a, 2014a, 2014b, 2015a, 2015b; Zhang et

137 al. 2021; Gao et al. 2023). In particular, the complete acidity constants on edge

138 surfaces of the trans-vacant TOT layer have been calculated by Liu et al.(Liu et al.

139 2013a, 2014a, 2015a, 2015b) In our recent study, the method was also successfully

140 applied to the edge surfaces of non-substituted and Mg-substituted cis-vacant TOT

141 layer (Gao et al. 2023). The pKa values of surface OH groups of oxides and

142 hydroxides have also been successfully derived using the same method (Cheng and

143 Sprik 2010; Liu et al. 2013b, 2014b; Zhang et al. 2021).

144   In this study, we calculated the pKa values for sites on surfaces perpendicular to

145 [010], [0$\bar{1}$0], [110] and [$\bar{1}\bar{1}$0] of 2:1-type Fe(II)/Fe(III) and Al(III) substituted

146 cis-vacant clay mineral. By combining the previous acidity values from the

147 non-substituted and the Mg-substituted cis-vacant TOT layer, we established a

148 complete surface acidity dataset for cis-vacant TOT layers. All atomic-level acidity

149 constants were then applied to construct SCMs and predict the acid-base titration data

150 without adjustable parameters, satisfying the principle of parsimony.

151 **METHODOLOGY**

152 **Models**

153   The primitive unit cell of cis-vacant 2:1 dioctahedral montmorillonite was taken

154 from our previous study (Gao et al. 2023). The Fe and Al substituted edge surface

155 models containing two unit cells were placed in 3D periodically repeated

7

156   orthorhombic boxes (12.45 Å × 10.44 Å × 33.56Å). The models included the surfaces

157   perpendicular to [010], [0$\bar{1}$0], [110] and [$\bar{1}$10] directions. 130 water molecules were

158   filled into the solution region of 20 Å which can approximate the density of bulk

159   water at ambient conditions according to previous reports (Gao et al. 2023). Ten water

160   molecules were inserted into the interlayer to create a monolayer hydrate.

161   Octahedral Fe(II) substitution (Fe$_{II}$-sub), octahedral Fe(III) substitution

162   (Fe$_{III}$-sub), and tetrahedral Al(III) substitution (Al-sub) on four edge surface directions

163   were all investigated (Fig. 2a-2d). Surfaces perpendicular to [110] and [$\bar{1}$10] are

164   beveled surfaces with different silanol groups, *i.e.* silanol on the upper tetrahedral

165   sheet and the lower tetrahedral sheet. Also, we only considered the cases where Al(III)

166   substitution occurs in the upper tetrahedral sheet on surfaces perpendicular to [110]

167   and [$\bar{1}$10] directions (Fig. 2g and 2h).

First-principles molecular dynamics

169   The computational model was carried out using density functional theory (DFT)

170   with the gradient-corrected functional of Perdew-Burke-Ernzerhof (PBE) (Perdew et

171   al. 1997) as implemented in the CP2K/Quickstep package. In this package, the

172   electronic structures were calculated with the hybrid Gaussian and Plane Wave (GPW)

173   approach (Lippert et al. 1997). A double-ζ atom-centered Gaussian-type basis with

174   polarization functions (DZVP)(VandeVondele and Hutter 2007) was used to construct

175   the electronic wave functions with 400 Ry energy cutoff and the core electrons

176   represented by Goedecker-Teter-Hutter (GTH) pseudopotentials (Goedecker et al.

177   1996). The dispersion correction was applied in all the calculations with the

178   Grimme-D3 method (Grimme et al. 2010, 2011). The Hubbard U correction for Fe

179   does not have an obvious influence on the pKa estimate for such systems (Zhang et al.

180   2021). The simulations were carried out with a multiplicity $(2S + 1)_{Fe(II)} = 5$ for

181   systems with a ferrous iron and $(2S + 1)_{Fe(III)} = 6$ for systems with a ferric iron,

182   respectively.

183   Born-Oppenheimer molecular dynamics (BOMD) simulations were carried out

184   within the canonical ensemble (NVT) controlled by a Nóse-Hoover chain thermostat

185   with a time step of 0.5 fs.(Martyna et al. 1992) In each step, the wave functions were

186   optimized to a tolerance of 10^{-6}. The temperature was controlled at 300 K. For each

187   system, we conducted an initial equilibration simulation of 3.0 ps, followed by a

188   production period of 5.0~10.0 ps.

189   **Acidity constant calculations**

190   The intrinsic pK_a values of the edge surface sites were evaluated with the

191   half-reaction scheme of the vertical energy gap method (Costanzo et al. 2011; Cheng

192   et al. 2014). In this method, the dissociating surface proton is gradually transformed

193   into a dummy atom, and the free energy is calculated using the thermodynamic

194   integration relation. The details are given in the Supporting Information.

195   The pKa values of the local and adjacent surface sites of substitution site on

196   surfaces perpendicular to [010], [0$\bar{1}$0], [110] and [$\bar{1}\bar{1}$0] were investigated. The surface

197   amphoteric sites of the Fe$_{II}$/Fe$_{III}$-sub model include $\equiv$Si(OH), $\equiv$Al(OH$_2$), $\equiv$Al(OH$_2$)$_2$,

198    $\equiv$Al(OH)(OH$_2$), $\equiv$Fe$_{II/III}$(OH$_2$)$_2$, $\equiv$Fe$_{II/III}$(OH)(OH$_2$), $\equiv$Si(OH)$_2$Fe$_{II/III}$, $\equiv$Si(O)(OH)Fe$_{II/III}$

199   and $\equiv$Si/Fe$_{II/III}$(OH)Al sites, while the surface amphoteric sites of the Al-sub model

9

200   include $\equiv Si(OH)$, $\equiv Al^T(OH_2)$, $\equiv Al^T(OH)$, $\equiv Al^T(OH)_2Al$, $\equiv Al^T(O)(OH)Al$, $\equiv Al(OH_2)_2$,

201    $\equiv Al(OH)(OH_2)$, $\equiv Al(OH_2)$ and $\equiv Al^T(OH)Al$ sites. Protons in some acidic sites

202   spontaneously dissociated within a few ps, such as $\equiv Si(OH)_2Fe$, $\equiv Fe(OH_2)_2$ and

203    $\equiv Al(OH_2)_2$ in the Fe_{III}-sub system, and therefore the OH bonds of these sites were

204   restrained with a harmonic potential in the calculation. For most sites in the Fe_{II}-sub

205   system, the deprotonated form would capture a proton from the solvent water

206   molecules. To prevent that from happening, all OH bonds in the water molecules were

207   restrained in the calculation.

208   **Surface complexation modeling**

209   An in-house version of PHREEQC which considers the spillover of electrostatic

210   potential from basal surfaces was used to calculate the protonation state of clay layer

211   edge surfaces (Parkhurst and Appelo 2013; Tournassat et al. 2016, 2018). The source

212   code modification is available in Tournassat et al. (2016). PHREEQC scripts and

213   database are available in the Supplementary Information.

214   **RESULTS AND DISCUSSION**

215   **FPMD simulations**

216   The energy gaps and deprotonation-free energies were listed in Tables S4-S6.

217   The calculated vertical energy gaps were well converged within 0.08 eV and the

218   statistical errors for pKa were smaller than 1.5 pKa units for all surface groups. The

219   uncertainties of the pKa value were evaluated with the semi-difference method.

220   Similar to the Mg(II)-substituted model in our previous report (Gao et al. 2023), the

221   surface sites of the Fe_{II}/Fe_{III} sub-model on surfaces perpendicular to $[0\bar{1}0]$ and $[110]$

222   are identical to the non-substituted model because the substituted cis-octahedron is

223   inside the bulk phase (Fig. 2b and 2c), while the surface sites on surfaces

224   perpendicular to [010] and [$\overline{1}10$] are altered (e.g., $\equiv Fe_{II/III}(OH_2)_2$ and $\equiv Si(OH)_2Fe_{II/III}$

225   sites) (Fig. 2a and 2d). In the Al-sub model, there is an additional specific site of

226    $\equiv Al^T(OH_2)$ compared to the non-substituted model. Because the influence of

227   isomorphic substitution on surface pKa values is usually limited in one unit cell (Liu

228   et al. 2014a, 2015a; Gao et al. 2023), the properties of the opposite $\equiv Si(OH)$ group

229   were not calculated in the Al-sub model.

230   *Acidity constant of Fe_{II}/Fe_{III} sub-models*

231   For the reduced Fe_{II} sub-model, the $\equiv Si(OH)$ sites on surfaces perpendicular to

232   the [010], [$0\overline{1}0$], [110] and [$\overline{1}10$] had high pKa values (Table S5), which was similar

233   to the silanol on Fe(II) substituted trans-vacant model (Liu et al. 2015a). The results

234   suggested that the substitution of Fe(II) led to an increase in the pKa value of the

235   adjacent $\equiv Si(OH)$ site to the extent that it would remain protonated in water. On the

236   surface perpendicular to [010], the vacancy sites $\equiv Si(OH)_2Fe_{II}$ and $\equiv Si(O)(OH)Fe_{II}$

237   had higher pKa values of 13.2 and 17.2, respectively, and therefore did not dissociate

238   under ambient pH conditions. Furthermore, the pKa values of $\equiv Al(OH_2)_2$ site on the

239   edge perpendicular to [$0\overline{1}0$] and of $\equiv Al(OH_2)$ site on the edge perpendicular to [110]

240   were similar (10.2 *versus* 10.7). These pKa values were also similar to the values of

241   the $\equiv Fe_{II}(OH_2)_2$ site on the surface perpendicular to [$\overline{1}10$] in the cis-vacant model

242   (10.9) as well as in the trans-vacant model (*i.e.* pKa of 10.2) (Liu et al. 2015a). In

243   addition, the pKa value of the $\equiv Si(OH)Al$ site on the surface perpendicular to [110]

11

244   was -7.7, indicating that it was unstable in water and this site remained dissociated.

245   For the structural OH groups, the pKa values of the $\equiv Fe_{II}(OH)Al$ site were 20.1 and

246   19.8 on surfaces perpendicular to $[0\bar{1}0]$ and $[\bar{1}\bar{1}0]$ respectively, both of which

247   remained non-reactive.

248   In the Fe_{III}-sub model, $\equiv Si(OH)_2Fe_{III}$ and $\equiv Si(O)(OH)Fe_{III}$ sites on the edge

249   perpendicular to [010] had pKa values of -0.4 and 5.7 (Table S5), which were close to

250   the $\equiv Si(OH)_2Al$ and $\equiv Si(O)(OH)Al$ sites of the non-substituted model (pKa of -0.8

251   and 5.9) (Gao et al. 2023). However, on the surface perpendicular to $[0\bar{1}0]$, the

252   $\equiv Al(OH_2)_2$ site had a much lower pKa value than in the non-substituted model (-0.1

253   and 5.7 respectively), while the pKa values of $\equiv Al(OH)(OH_2)$ and $\equiv Fe_{III}(OH)Al$ were

254   also decreased to 6.1 and 8.9, respectively. On the surface perpendicular to [110],

255   $\equiv Si(OH)Al$ and $\equiv Al(OH_2)$ had pKa values of -14.6 and 2.7, which suggested that the

256   protonated forms were not stable at environmentally relevant pH values. The pKa

257   values of $\equiv Fe_{III}(OH_2)_2$ and $\equiv Fe_{III}(OH)(OH_2)$ on surface perpendicular to $[\bar{1}\bar{1}0]$ were

258   -7.7 and 2.3, respectively. Moreover, the pKa value of the $\equiv Fe_{III}(OH)Al$ site on the

259   surface perpendicular to $[\bar{1}\bar{1}0]$ closely resembled the same site on the surface

260   perpendicular to $[0\bar{1}0]$ with a pKa value of 8.7 (vs 8.9). The pKa values of the $\equiv Si(OH)$

261   site on surfaces perpendicular to [010], $[0\bar{1}0]$, [110] and $[\bar{1}\bar{1}0]$ of the $\equiv Fe_{III}$-sub model

262   were all increased by 0.0~2.0 pKa units compared to the non-substituted model (Table

263   S6) (Gao et al. 2023). Considering the computational error, it is difficult to state

264   unequivocally that Fe(III)-substitution affects the neighboring silanol site. But from

265   another perspective, compared to the acidity constants obtained with the Fe_{II}-sub

266   model, Fe oxidation (Fe$_{III}$-sub) decreased the pKa values of the counterpart sites,

267   which was consistent with results obtained previously with a trans-vacant model (Liu

268   et al. 2015a).

269   *Acidity constant of Al-sub model*

270   The calculated pKa values of tetrahedral $\equiv Al^T(OH_2)$ and $\equiv Al^T(OH)$ sites on the

271   edge perpendicular to [010] were 3.1 and 14.0, respectively. The lower pKa value of

272   the $\equiv Al^T(OH_2)$ site indicated that it rarely occurred in the normal pH range. In

273   addition, the pKa values of $\equiv Al^T(OH_2)/\equiv Al^T(OH)$ were 2.9/14.2, 3.0/14.5, and

274   1.5/14.4 on surfaces perpendicular to [0$\bar{1}$0], [110] and [$\bar{1}\bar{1}$0], while on the trans-vacant

275   surfaces perpendicular to [010] and [110] the pKa values were -2.4/15.1 and -2.4/17.5,

276   respectively (Liu et al. 2014a). Hence, similar results were obtained for all

277      $\equiv Al^T(OH_2)/\equiv Al^T(OH)$ sites. On the surface perpendicular to [010], $\equiv Al^T(OH)_2Al$ and

278      $\equiv Al^T(O)(OH)Al$ site had pKa values of 7.1 and 16.1, suggesting that $\equiv Al^T(O)(OH)Al$

279   was the dominant surface species under environmentally relevant conditions. As

280   shown in Fig. 3, octahedral $\equiv Al(OH_2)_2$ and $\equiv Al(OH)(OH_2)$ site on surfaces

281   perpendicular to [0$\bar{1}$0] and [$\bar{1}\bar{1}$0] were 7.8/11.0 and 6.0/9.7, respectively, which were

282   similar to the pKa values of the counterpart site on the surface perpendicular to [0$\bar{1}$0]

283   of the non-substituted model (5.7/9.8) (Gao et al. 2023), indicating a weak influence

284   of Al(III) substitution. Bridging sites $\equiv Al^T(OH)Al$ on the surface perpendicular to

285   [110] exhibited a pKa value of 6.9, which was different from other substitution cases

286   of the $\equiv Si(OH)Al$ site having a very low pKa value (-7.7 for the Fe$_{II}$-sub model, -14.6

287   for the Fe$_{III}$-sub model, -7.1 for the Mg-sub model and -11.7 for the No-sub model)

288   (Liu et al. 2014a, 2015a; Gao et al. 2023). On the other hand, the $\equiv Al^T(OH)Al$ site

289   could participate in acid-base reactions in the common pH range and was similar to

290   the sites on the surface perpendicular to [110] in an Al(III)-substituted trans-vacant

291   model (Liu et al. 2014a). Furthermore, the pKa value of the $\equiv Al(OH_2)$ site on the

292   surface perpendicular to [110] was also increased to 10.4 compared to 5.6 of the

293   non-substituted model (Gao et al. 2023).

Summary of acidity constant values

295   From the above analysis, the Fe(III) substitution decreased the pKa values at the

296   local sites while iron reduction (Fe(II) substitution) increased significantly the pKa

297   values at the local and adjacent sites. Such influence of Fe(II) substitution was similar

298   to that of Mg-substitution in trans- and cis-vacant structures (Gao et al. 2023). Al(III)

299   substitution generated a reactive site $\equiv Al^T(OH_2)$ in the ambient pH condition. In

300   addition, the effect of the Al(III) substitution on neighboring sites was weak, however,

301   the effect on the acidity of the bridging site ($\equiv Al^T(OH)Al$, $\equiv Al^T(OH)_2Al$ and

302    $\equiv Al^T(O)(OH)Al$ sites) was particularly significant. This phenomenon was similar to

303   that found in the trans-vacant model (Liu et al. 2014a).

304   Table 1 summarizes the pKa values calculated in this study as well as the results

305   obtained previously for non- and Mg-substituted cis-vacant TOT layer and

306   trans-vacant TOT layer. This database can be used for further modeling studies of

307   natural montmorillonites, which contain various substitutions.

Predicted SCMs for potentiometric titration data

309   Tournasssat et al. developed prediction models for acid-base titration data of

14

310   MX80 and Swy-2 montmorillonite, in which the acidity constants were based on the

311   trans-vacant model (Tournassat et al. 2016). Our previous study (Gao et al. 2023)

312   also used non-substituted and Mg-substituted cis-vacant surface acidity constants to

313   predict published potentiometric titration data with identical model parameters and

314   calculation procedures as in Tournassat et al. (2016). Both prediction models were in

315   reasonable agreement with the experimental data. The edge-specific surface area is

316   not a well-defined parameter in clay SCMs. Among surface area measurement

317   techniques, the derivative isotherms summation (DIS) method tends to overestimate

318   the surface area (Reinholdt et al. 2013), whereas the atomic force microscopy (AFM)

319   method may provide a more accurate estimate of surface area for montmorillonite

320   (Tournassat et al. 2003; Cadene et al. 2005; Kraevsky et al. 2020; Orucoglu et al.

321   2022). The AFM-measured edge-specific surface area was 9 $m^2 \cdot g^{-1}$ for MX80

322   montmorillonite (Tournassat et al. 2015), while the specific surface area used in the

323   model was 12 $m^2 \cdot g^{-1}$ (Tournassat et al. 2016; Gao et al. 2023). These edge-specific

324   surface area values may however be dependent on the clay material preparation

325   method, which includes a granulometric separation step that can lead to different

326   particle size distributions depending on the exact preparation method.

327   Complete acidity constants of the cis-vacant model were used to predict

328   potentiometric titration data of MX80 and Swy-2 montmorillonites (Duc et al.

329   2005b). The edge-specific surface area of the cis-vacant model was fitted to

330   reproduce potentiometric titration data (Fig. S1). The agreement between

331   experimental and fitted potentiometric titration curves was acceptable if the specific

332   edge surface areas were set to 9 m^2·g^{-1} and the relative abundance of cis-vacant

333   edges perpendicular to [010], [0$\bar{1}$0], [110], and [$\bar{1}\bar{1}$0] was set at 0.15/0.15/0.35/0.35

334   for both MX80 and Swy-2 montmorillonites, which is similar to experimental AFM

335   results (Kraevsky et al. 2020) as well as with a distribution of edge orientations in a

336   pseudo-hexagonal clay particle. Fig. 4 includes also the comparison of predictions

337   based on the cis- and trans-vacant models. For the latter, the relative abundance of

338   trans-vacant edges perpendicular to [010] and [110] was set at 0.3/0.7 and the

339   edge-specific surface areas were set to 14 m^2·g^{-1} and 12 m^2·g^{-1} for Swy-2 and MX80

340   montmorillonites, respectively. A good agreement was found between experimental

341   and fitted potentiometric titration data with both cis- and trans-vacant models, but,

342   for Swy-2 montmorillonite, a better agreement was found with the cis-vacant model

343   at pH above 6.0. For MX80 montmorillonite, the cis- and trans-vacant model

344   predictions were very similar.

345   With the complete consideration of clay isomorphic substitution cases, the

346   surface potentials on surfaces perpendicular to [010], [0$\bar{1}$0], [110], and [$\bar{1}\bar{1}$0] of the

347   trans-vacant model and surfaces perpendicular to [010] and [110] of the cis-vacant

348   model were predicted to be negative (Fig. S2). Contrastingly, with the cis-vacant

349   model, surfaces perpendicular to [010] and [110] directions were predicted to have a

350   positive potential below pH 6-7, as already predicted with a cis-vacant model without

351   isomorphic substitution (Gao et al. 2023).

352   In our SCMs, only one parameter was adjusted: the edge-specific surface area.

353   Its fitted value was in good agreement with values measured on a similar clay material

354   using AFM. Other parameters were fully constrained using experimental data and

355   ab-initio calculations, including the distribution of edge surface orientations, the solid

356   concentration, the nature and amount of isomorphic substitutions in the clay layer, and

357   the acidity constants.

358   **IMPLICATIONS**

359   Our complete set of acidity constants for 2:1 TOT layers enables predictive

360   modeling of the interfacial properties for a wide range of clay minerals. Table 2

361   listed the structural formulas of some trans- or cis-vacant clay minerals, which

362   include various substitutions. The predicted potentiometric titration and surface

363   charge curves for these minerals are shown in Fig. 5. The modeling results indicated

364   that the extent of the various isomorphic substitutions (tetrahedral vs. octahedral and

365   Fe vs. Mg in octahedral position) had little influence on the predicted titration curves.

366   Contrastingly, the consideration of cis-vacant vs. trans-vacant structures led to

367   significant differences in surface charge at pH above pH 8.0. This study highlights

368   the importance of considering the local structure of clay minerals to fully understand

369   their reactivity. To obtain accurate pKa values, complete atomic-level information

370   based on the real structure of natural montmorillonite is necessary. Overall, this work

371   achieved a comprehensive study of the acid-base properties of cis-vacant clay edge

372   surfaces concerning layer chemistry and structure, which provides fundamental

373   information for the modeling of contaminant adsorption on natural clay minerals.

17

387   **REFERENCES CITED**

388   Baeyens, B., and Bradbury, M.H. (1997) A mechanistic description of Ni and Zn sorption on
389   Na-montmorillonite part I: Titration and sorption measurements. Journal of Contaminant
390   Hydrology, 27, 199–222.

391   Bergaya, F., and Lagaly, G. (2006) Chapter 1 General introduction: Clays, clay minerals, and clay
392   science. In Faïza Bergaya, B.K.G. Theng, and Gerhard Lagaly, Eds., Developments in
393   Clay Science Vol. 1, pp. 1–18. Elsevier.

394   Bergaya, F., Theng, B.K.G., and Lagaly, G. (2006) Chapter 12 Critical assessment of some
395   analytical techniques. In Faïza Bergaya, Benny K.G. Theng, and Gerhard Lagaly, Eds.,
396   Developments in Clay Science Vol. 1, pp. 753–754. Elsevier.

397   Bourg, I.C., Sposito, G., and Bourg, A.C.M. (2007) Modeling the acid–base surface chemistry of
398   montmorillonite. Journal of Colloid and Interface Science, 312, 297–310.

399   Brigatti, M.F., Galan, E., and Theng, B.K.G. (2006) Chapter 2 Structures and mineralogy of clay
400   minerals. In F. Bergaya, Benny K.G. Theng, and G. Lagaly, Eds., Developments in Clay
401   Science Vol. 1, pp. 19–86. Elsevier.

402   Brigatti, M.F., Malferrari, D., Laurora, A., and Elmi, C. (2011) Structure and mineralogy of layer
403   silicates: recent perspectives and new trends. In M.F. Brigatti and A. Mottana, Eds.,
404   Layered Mineral Structures and their Application in Advanced Technologies pp. 1–71.
405   Mineralogical Society of Great Britain and Ireland, London.

406   Cadene, A., Durand-Vidal, S., Turq, P., and Brendle, J. (2005) Study of individual
407   Na-montmorillonite particles size, morphology, and apparent charge. Journal of Colloid
408   and Interface Science, 285, 719–730.

409   Cases, J.M., Berend, I., Besson, G., Francois, M., Uriot, J.P., Thomas, F., and Poirier, J.E. (1992)
410   Mechanism of adsorption and desorption of water vapor by homoionic montmorillonite. 1.
411   The sodium-exchanged form. Langmuir, 8, 2730–2739.

412   Charlet, L., Schindler, P.W., Spadini, L., Furrer, G., and Zysset, M. (1993) Cation adsorption on
413   oxides and clays: The aluminum case. Aquatic Sciences, 55, 291–303.

414   Cheng, J., and Sprik, M. (2010) Acidity of the Aqueous Rutile TiO $_2$ (110) Surface from Density
415   Functional Theory Based Molecular Dynamics. Journal of Chemical Theory and
416   Computation, 6, 880–889.

417   Cheng, J., Liu, X., VandeVondele, J., Sulpizi, M., and Sprik, M. (2014) Redox potentials and
418   acidity constants from density functional theory based molecular dynamics. Accounts of
419   Chemical Research, 47, 3522–3529.

420   Costanzo, F., Sulpizi, M., Valle, R.G.D., and Sprik, M. (2011) The oxidation of tyrosine and
421   tryptophan studied by a molecular dynamics normal hydrogen electrode. The Journal of
422   Chemical Physics, 134, 244508.

423   Davis, J.A., James, R.O., and Leckie, J.O. (1978) Surface ionization and complexation at the
424   oxide/water interface. Journal of Colloid and Interface Science, 63, 480–499.

425   Drits, V.A., and Zviagina, B.B. (2009) *Trans*-vacant and *cis*-vacant 2:1 layer silicates: Structural
426   features, identification, and occurrence. Clays and Clay Minerals, 57, 405–415.

427   Duc, M., Gaboriaud, F., and Thomas, F. (2005a) Sensitivity of the acid–base properties of clays to
428   the methods of preparation and measurement：1. Literature review. Journal of Colloid and
429   Interface Science, 289, 139–147.

430   ——— (2005b) Sensitivity of the acid–base properties of clays to the methods of preparation and
431   measurement：2. Evidence from continuous potentiometric titrations. Journal of Colloid
432   and Interface Science, 289, 148–156.

433   Duc, M., Thomas, F., and Gaboriaud, F. (2006) Coupled chemical processes at clay/electrolyte
434   interface: A batch titration study of Na-montmorillonites. Journal of Colloid and Interface
435   Science, 300, 616–625.

436   Duc, M., Carteret, C., Thomas, F., and Gaboriaud, F. (2008) Temperature effect on the acid–base
437   behaviour of Na-montmorillonite. Journal of Colloid and Interface Science, 327, 472–
438   476.

439   Gailhanou, H., Blanc, P., Rogez, J., Mikaelian, G., Kawaji, H., Olives, J., Amouric, M., Denoyel,
440   R., Bourrelly, S., Montouillout, V., and others (2012) Thermodynamic properties of illite,
441   smectite and beidellite by calorimetric methods: Enthalpies of formation, heat capacities,
442   entropies and gibbs free energies of formation. Geochimica et Cosmochimica Acta, 89,
443   279–301.

444   Gao, P., Liu, X., Guo, Z., and Tournassat, C. (2023) Acid–base properties of cis-vacant
445   montmorillonite edge surfaces: A combined first-principles molecular dynamics and
446   surface complexation modeling approach. Environmental Science & Technology, 1342–
447   1352.

448   Gates, W.P., Slade, P.G., Manceau, A., and Lanson, B. (2002) Site Occupancies by Iron in
449   Nontronites. Clays and Clay Minerals, 50, 223–239.

450   Goedecker, S., Teter, M., and Hutter, J. (1996) Separable dual-space gaussian pseudopotentials.
451   Physical Review B, 54, 1703–1710.

452   Grimme, S., Antony, J., Ehrlich, S., and Krieg, H. (2010) A consistent and accurate *ab initio*
453   parametrization of density functional dispersion correction (DFT-D) for the 94 elements
454   H-Pu. The Journal of Chemical Physics, 132, 154104.

455   Grimme, S., Ehrlich, S., and Goerigk, L. (2011) Effect of the damping function in dispersion
456   corrected density functional theory. Journal of Computational Chemistry, 32, 1456–1465.

457   Kéri, A., Dähn, R., Krack, M., and Churakov, S.V. (2017) Combined XAFS spectroscopy and ab
458   initio study on the characterization of iron incorporation by montmorillonite.
459   Environmental Science & Technology, 51, 10585–10594.

460   Kome, G.K., Enang, R.K., Tabi, F.O., and Yerima, B.P.K. (2019) Influence of clay minerals on
461   some soil fertility attributes: A review. Open Journal of Soil Science, 09, 155–188.

462   Kraevsky, S.V., Tournassat, C., Vayer, M., Warmont, F., Grangeon, S., Ngouana Wakou, B.F., and
463   Kalinichev, A.G. (2020) Identification of montmorillonite particle edge orientations by

464   atomic-force microscopy. Applied Clay Science, 186, 105442.

465 Lagaly, G. (2006) Chapter 5 - Colloid clay science. In F. Bergaya, B.K.G. Theng, and Gerhard

466   Lagaly, Eds., Developments in Clay Science Vol. 1, pp. 141–245. Elsevier.

467 Lantenois, S., Muller, F., Bény, J.-M., Mahiaoui, J., and Champallier, R. (2008) Hydrothermal

468   synthesis of beidellites: bharacterization and study of the cis- and trans-Vacant Character.

469   Clays and Clay Minerals, 56, 39–48.

470 Leung, K., and Criscenti, L.J. (2012) Predicting the acidity constant of a goethite hydroxyl group

471   from first principles. Journal of Physics: Condensed Matter, 24, 124105.

472 Leung, K., Nielsen, I.M.B., and Criscenti, L.J. (2009) Elucidating the bimodal acid−base behavior

473   of the water−silica interface from first principles. Journal of the American Chemical

474   Society, 131, 18358–18365.

475 Lippert, G., Hutter, J., and Parrinello, M. (1997) A hybrid Gaussian and plane wave density

476   functional scheme. Molecular Physics, 92, 477–488.

477 Liu, X., Lu, X., Sprik, M., Cheng, J., Meijer, E.J., and Wang, R. (2013a) Acidity of edge surface

478   sites of montmorillonite and kaolinite. Geochimica et Cosmochimica Acta, 117, 180–190.

479 Liu, X., Cheng, J., Sprik, M., Lu, X., and Wang, R. (2013b) Understanding surface acidity of

480   gibbsite with first principles molecular dynamics simulations. Geochimica et

481   Cosmochimica Acta, 120, 487–495.

482 ——— (2014a) Surface acidity of 2:1-type dioctahedral clay minerals from first principles

483   molecular dynamics simulations. Geochimica et Cosmochimica Acta, 140, 410–417.

484 Liu, X., Cheng, J., Lu, X., and Wang, R. (2014b) Surface acidity of quartz: understanding the

485   crystallographic control. Phys. Chem. Chem. Phys., 16, 26909–26916.

486 Liu, X., Cheng, J., Sprik, M., Lu, X., and Wang, R. (2015a) Interfacial structures and acidity of

487   edge surfaces of ferruginous smectites. Geochimica et Cosmochimica Acta, 168, 293–

488   301.

489 Liu, X., Lu, X., Cheng, J., Sprik, M., and Wang, R. (2015b) Temperature dependence of interfacial

490   structures and acidity of clay edge surfaces. Geochimica et Cosmochimica Acta, 160, 91–

491   99.

492 Liu, X., Tournassat, C., Grangeon, S., Kalinichev, A.G., Takahashi, Y., and Marques Fernandes, M.

493   (2022) Molecular-level understanding of metal ion retention in clay-rich materials. Nature

494   Reviews Earth & Environment, 3, 461–476.

495 Manceau, A., Lanson, B., Drits, V.A., Chateigner, D., Gates, W.P., Wu, J., Huo, D., and Stucki,

496   J.W. (2000) Oxidation-reduction mechanism of iron in dioctahedral smectites: 1. Crystal

497   chemistry of oxidized reference nontronites. American Mineralogist, 85, 133–152.

498 Martyna, G.J., Klein, M.L., and Tuckerman, M. (1992) Nosé–Hoover chains: The canonical

499   ensemble via continuous dynamics. The Journal of Chemical Physics, 97, 2635–2643.

500 Mccabe, R.W., and Adams, J.M. (2013) Chapter 4.3 - Clay minerals as catalysts. In F. Bergaya and

501   G. Lagaly, Eds., Developments in Clay Science Vol. 5, pp. 491–538. Elsevier.

502 Okada, T., Morita, T., and Ogawa, M. (2005) Tris(2,2'-bipyridine)ruthenium(II)-clays as

503   adsorbents for phenol and chlorinated phenols from aqueous solution. Applied Clay

504   Science, 29, 45–53.

505 Orucoglu, E., Grangeon, S., Gloter, A., Robinet, J.-C., Madé, B., and Tournassat, C. (2022)

506   Competitive adsorption processes at clay mineral surfaces: A coupled experimental and

507   modeling approach. ACS Earth and Space Chemistry, 6, 144–159.

508   Parkhurst, D.L., and Appelo, C.A.J. (2013) Description of input and examples for PHREEQC
509   Version 3-A computer program for speciation, batch-reaction, one-dimensional transport,
510   and inverse geochemical calculations, chapter A43, p 497, Book 6 p. U.S. Geological
511   Survey: Denver.
512   Perdew, J.P., Burke, K., and Ernzerhof, M. (1997) Generalized gradient approximation made
513   simple. Phys. Rev. Lett., 78, 1396–1396.
514   Reinholdt, M.X., Hubert, F., Faurel, M., Tertre, E., Razafitianamaharavo, A., Francius, G., Prêt, D.,
515   Petit, S., Béré, E., Pelletier, M., and others (2013) Morphological properties of
516   vermiculite particles in size-selected fractions obtained by sonication. Applied Clay
517   Science, 77–78, 18–32.
518   Schoonheydt, R.A., and Johnston, C.T. (2006) Chapter 3 Surface and interface chemistry of clay
519   minerals. In F. Bergaya, B.K.G. Theng, and G. Lagaly, Eds., Developments in Clay
520   Science Vol. 1, pp. 87–113. Elsevier.
521   Sposito, G., Skipper, N.T., Sutton, R., Park, S., Soper, A.K., and Greathouse, J.A. (1999) Surface
522   geochemistry of the clay minerals. Proceedings of the National Academy of Sciences, 96,
523   3358–3364.
524   Stucki, J.W. (2013) Chapter 11 - Properties and behaviour of iron in clay minerals. In F. Bergaya
525   and G. Lagaly, Eds., Developments in Clay Science Vol. 5, pp. 559–611. Elsevier.
526   Subramanian, N., Whittaker, M.L., Ophus, C., and Lammers, L.N. (2020) Structural implications
527   of interfacial hydrogen bonding in hydrated Wyoming-montmorillonite clay. The Journal
528   of Physical Chemistry C, 124, 8697–8705.
529   Sulpizi, M., Gaigeot, M.-P., and Sprik, M. (2012) The silica−water interface: How the silanols
530   determine the surface acidity and modulate the water properties. J. Chem. Theory
531   Comput., 8, 1037–1047.
532   Tazi, S., Rotenberg, B., Salanne, M., Sprik, M., and Sulpizi, M. (2012) Absolute acidity of clay
533   edge sites from ab-initio simulations. Geochimica et Cosmochimica Acta, 94, 1–11.
534   Tombácz, E., and Szekeres, M. (2004) Colloidal behavior of aqueous montmorillonite suspensions:
535   the specific role of pH in the presence of indifferent electrolytes. Applied Clay Science,
536   27, 75–94.
537   ——— (2006) Surface charge heterogeneity of kaolinite in aqueous suspension in comparison
538   with montmorillonite. Applied Clay Science, 34, 105–124.
539   Tournassat, C., Neaman, A., Villiéras, F., Bosbach, D., and Charlet, L. (2003) Nanomorphology of
540   montmorillonite particles: Estimation of the clay edge sorption site density by
541   low-pressure gas adsorption and AFM observations. American Mineralogist, 88, 1989–
542   1995.
543   Tournassat, C., Bourg, I.C., Steefel, C.I., and Bergaya, F. (2015) Chapter 1 - Surface properties of
544   clay minerals. In C. Tournassat, C.I. Steefel, I.C. Bourg, and Faqpza Bergaya, Eds.,
545   Developments in Clay Science Vol. 6, pp. 5–31. Elsevier.
546   Tournassat, C., Davis, J.A., Chiaberge, C., Grangeon, S., and Bourg, I.C. (2016) Modeling the
547   Acid–Base Properties of Montmorillonite Edge Surfaces. Environmental Science &
548   Technology, 50, 13436–13445.
549   Tournassat, C., Tinnacher, R.M., Grangeon, S., and Davis, J.A. (2018) Modeling uranium(VI)
550   adsorption onto montmorillonite under varying carbonate concentrations: A surface
551   complexation model accounting for the spillover effect on surface potential. Geochimica

552   et Cosmochimica Acta, 220, 291–308.

553   Tsipursky, S.I., and Drits, V.A. (1984) The distribution of octahedral cations in the 2:1 layers of

554   dioctahedral smectites studied by oblique-texture electron diffraction. Clay Minerals, 19,

555   177–193.

556   VandeVondele, J., and Hutter, J. (2007) Gaussian basis sets for accurate calculations on molecular

557   systems in gas and condensed phases. The Journal of Chemical Physics, 127, 114105.

558   Wanner, H., Albinsson, Y., Karnland, O., Wieland, E., Wersin, P., and Charlet, L. (1994) The

559   acid/base chemistry of montmorillonite. Radiochimica Acta, 66/67, 157–162.

560   Zhang, Y., Liu, X., Cheng, J., and Lu, X. (2021) Interfacial structures and acidity constants of

561   goethite from first-principles Molecular Dynamics simulations. American Mineralogist,

562   106, 1736–1743.

563   Zysset, M., and Schindler, P.W. (1996) The proton promoted dissolution kinetics of

564   K-montmorillonite. Geochimica et Cosmochimica Acta, 60, 921–931.

565

566 **TABLE 1.** Summary of complete pKa values of edge sites on individual surfaces of
567 trans/cis-vacant models (*tv* and *cv*, respectively)

	Sites	$cv \perp [010]$	$cv \perp [0\bar{1}0]$	$cv \perp [110]$	$cv \perp [\bar{1}\bar{1}0]$	[a] $tv \perp [010]$	[a] $tv \perp [110]$
[b] No-sub	≡Si(OH)	6.8	8.1	$6.3^U/6.8^L$	$7.4^U/8.1^L$	7.0	$8.0^U/8.3^L$
	≡Al(OH$_2$)$_2$/≡Al(OH)(OH$_2$)	—	5.7/9.8	—	7.0/—	3.1/8.3	—
	≡Al(OH$_2$)	—	—	5.6	—	—	5.5
	≡Si(OH)Al	—	—	-11.7	—	—	1.7
	≡Si(OH)$_2$Al/≡Si(O)(OH)Al	-0.8/5.9	—	—	—	—	—
	≡Al(OH)Al	—	13.2	—	17.6	—	—
[b] Mg-sub	≡Si(OH)	9.0	11.0	$9.1^U/10.4^L$	$8.9^U/9.2^L$	10.8	11.0
	≡Mg(OH$_2$)$_2$	—	—	—	15.1	13.2	—
	≡Si(OH)Mg	—	—	—	—	—	4.2
	≡Al(OH$_2$)$_2$/≡Al(OH)(OH$_2$)	—	5.9/10.1	—	—	—	—
	≡Al(OH$_2$)	—	—	8.5	—	—	—
	≡Si(OH)Al	—	—	-7.1	—	—	—
	≡Si(OH)$_2$Mg/≡Si(O)(OH)Mg	5.3/8.8	—	—	—	—	—
	≡Mg(OH)Al	—	16.6	—	18.7	—	—
Fe$_{II}$-sub	≡Si(OH)	12.2	13.5	$13.8^U/12.7^L$	$12.3^U/11.4^L$	11.2	—
	≡Fe(OH$_2$)$_2$	—	—	—	10.9	10.2	—
	≡Al(OH$_2$)$_2$	—	10.2	—	—	—	—
	≡Al(OH$_2$)	—	—	10.7	—	—	—
	≡Si(OH)Al	—	—	-7.7	—	—	—
	≡Si(OH)$_2$Fe/≡Si(O)(OH)Fe	13.2/17.2	—	—	—	—	—
	≡Fe(OH)Al	—	20.1	—	19.8	—	—
Fe$_{III}$-sub	≡Si(OH)	8.8	9.0	$8.4^U/7.1^L$	$7.9^U/8.1^L$	8.6	—
	≡Fe(OH$_2$)$_2$/≡Fe(OH)(OH$_2$)	—	—	—	-7.7/2.3	1.2/5.1	—
	≡Al(OH$_2$)$_2$/≡Al(OH)(OH$_2$)	—	-0.1/6.1	—	—	—	—
	≡Al(OH$_2$)	—	—	2.7	—	—	—
	≡Si(OH)Al	—	—	-14.6	—	—	—
	≡Si(OH)$_2$Fe/≡Si(O)(OH)Fe	-0.4/5.7	—	—	—	—	—

	≡Fe(OH)Al	—	8.9	—	8.0	—	—
Al-sub	≡Al^T(OH$_2$)/ ≡Al^T(OH)	3.1/14.0	2.9/14.2	3.0/14.5	1.5/14.4	-2.4/15.1	-2.4/17.5
	≡Al(OH$_2$)$_2$/ ≡Al(OH)(OH$_2$)	—	7.8/11.0	—	6.0/9.7	4.9/8.5	—
	≡Al(OH$_2$)	—	—	10.4	—	—	12.7
	≡Al^T(OH)Al	—	—	6.9	—	—	10.2
	≡Al^T(OH)$_2$Al/ ≡Al^T(O)(OH)Al	7.1/16.1	—	—	—	—	—

568   [a] The pKa values of the trans-vacant model were taken from Liu et al. (Liu et al. 2014a, 2015a)

569   [b] The pKa values of the No-sub and Mg-sub cis-vacant model were taken from Gao et al. (Gao et

570   al. 2023)

571

572

573

574   **TABLE 2.** Structural formulas of some 2:1 type trans/cis-vacant (*tv/cv)* clay minerals.

| 2:1 Clay Samples	Structural Formulae	Model
Montmorillonite (Swy-1) (Cases et al. 1992)	$(Si_{3.91}Al_{0.09})(Al_{1.64}Mg_{0.25}Fe^{3+}_{0.08}Fe^{2+}_{0.08})Na_{0.37}O_{10}(OH)_2$	*cv*
Montmorillonite (Kunipia) (Okada et al. 2005; Orucoglu et al. 2022)	$(Si_{3.825}Al_{0.175})(Al_{1.64}Mg_{0.215}Fe^{3+}_{0.155})Na_{0.265}Ca_{0.045}O_{10}(OH)_2$	*cv*
Beidellite (SBId-1) (Lantenois et al. 2008; Gailhanou et al. 2012)	$(Si_{3.574}Al_{0.426})(Al_{1.812}Mg_{0.09}Fe^{3+}_{0.112})K_{0.104}Ca_{0.185}O_{10}(OH)_2$	*tv*
Beidellite (SB1-350) (Lantenois et al. 2008)	$(Si_{3.60}Al_{0.4})(Al_2)Na_{0.38}O_{10}(OH)_2$	*cv*
Nontronite (NG-1) (Manceau et al. 2000)	$(Si_{3.645}Fe^{3+}_{0.315}Al_{0.04})(Al_{0.44}Mg_{0.03}Fe^{3+}_{1.54}Fe^{2+}_{0.005})Na_{0.35}O_{10}(OH)_2$	*tv*
Nontronite (NAu-2) (Gates et al. 2002)	$(Si_{3.775}Fe^{3+}_{0.145}Al_{0.08})(Al_{0.17}Mg_{0.025}Fe^{3+}_{1.77})Na_{0.36}O_{10}(OH)_2$	*tv*

575

576

577
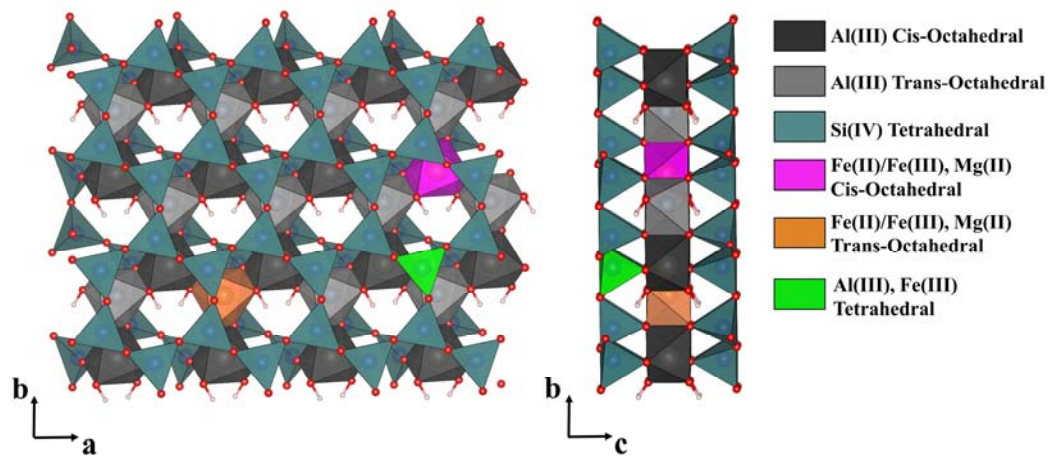
578 **FIGURE 1.** Views of the modeled cis-vacant TOT clay layer with substituted ions in the cis- and
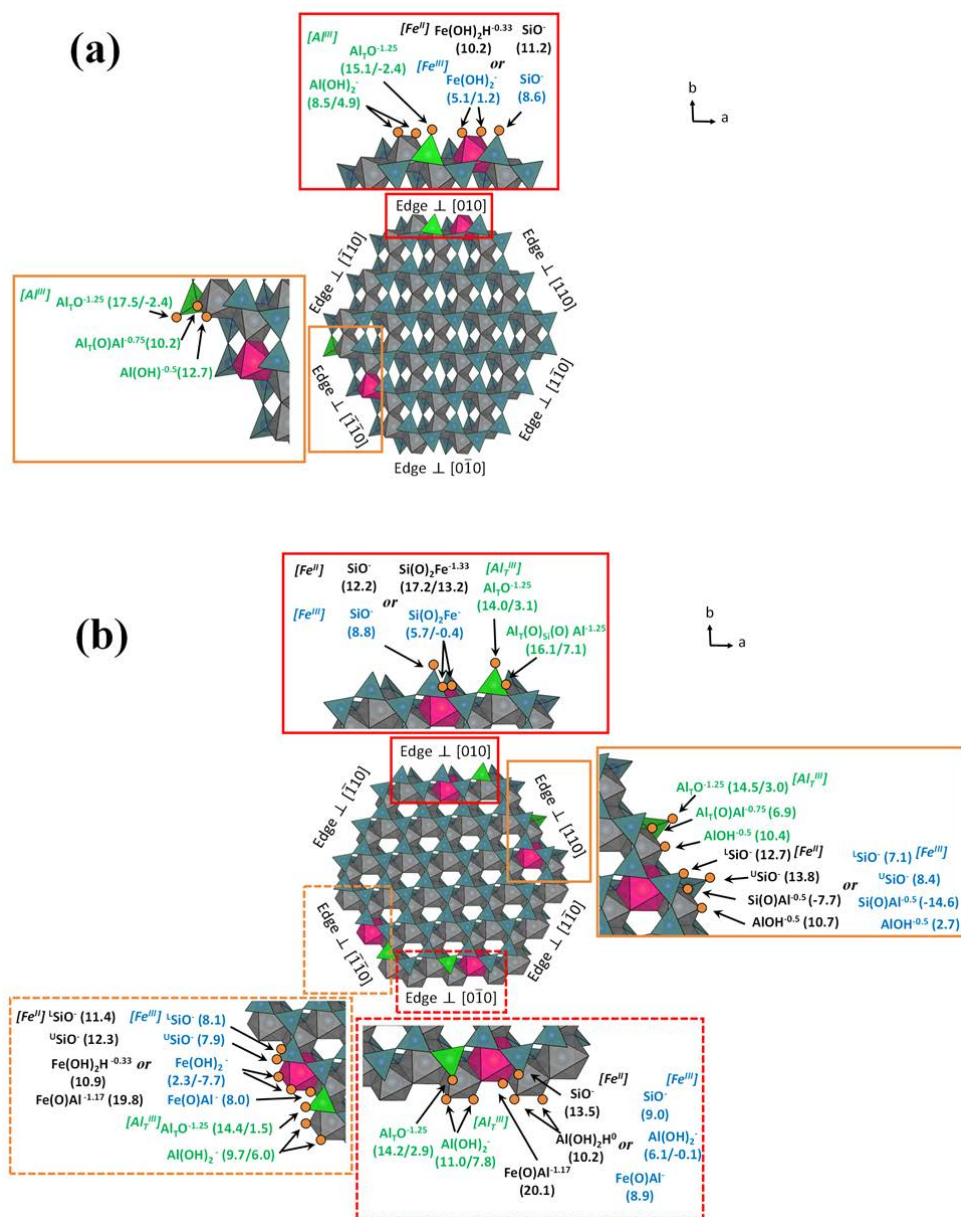579 trans-sites of the octahedral sheet and in the tetrahedral sheet.

580

581

582

Fe(II/III) substitution model　　　　**Al(III) substitution model**
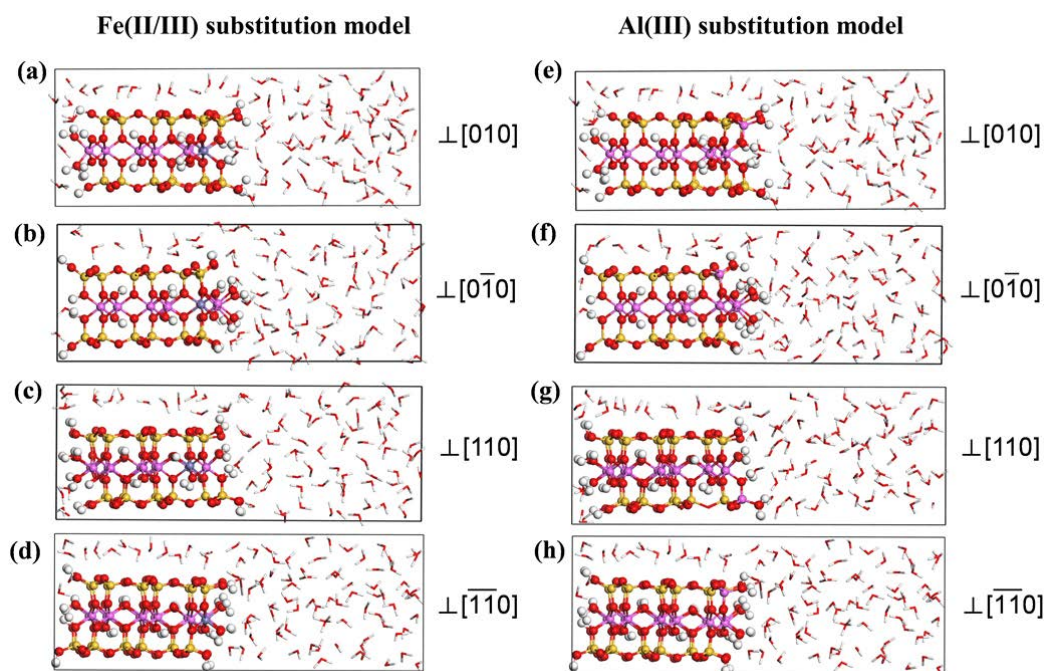
FIGURE 2. Edge surface models of Fe(II)/(III)-substituted (Fe$_{II/III}$-sub) and Al(III)-substituted

(Al-sub) cis-vacant structure. (a) and (e) ⊥[010], (b) and (f) ⊥[0$\bar{1}$0], (c) and (g) ⊥[110], (d)

and (h) ⊥[$\bar{1}\bar{1}$0]. Color scheme: Si (yellow), Al (pink), Fe (cyan), O (red), H (white).
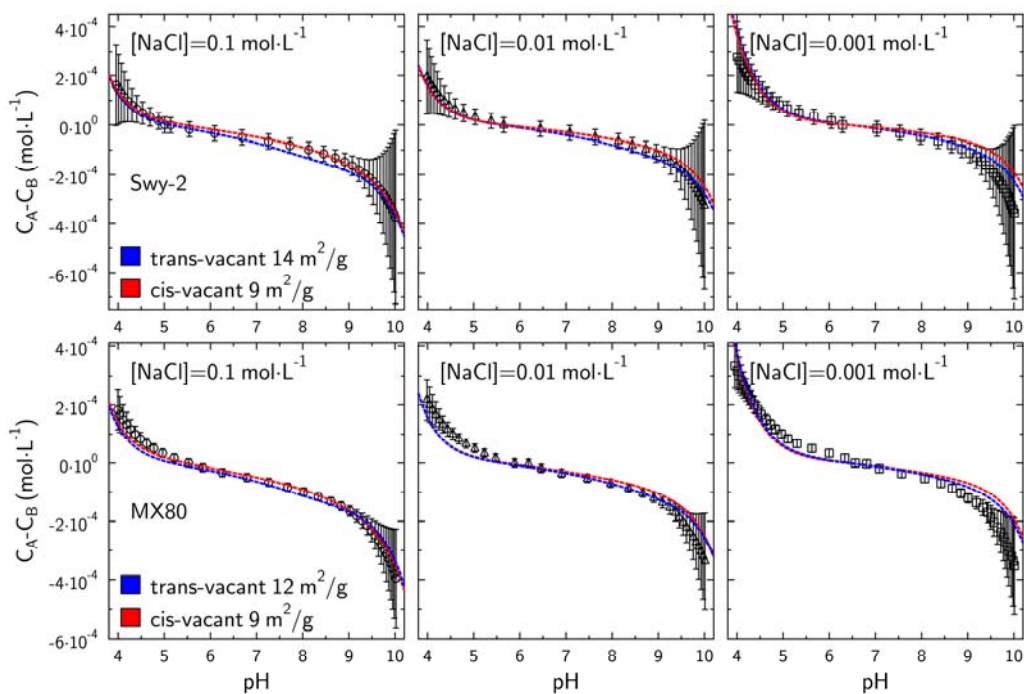
587

588

589

590 **FIGURE 3.** Edge surface sites and pKa values of Fe(II)/(III)- and Al(III)-substituted clay models.

591 (a) trans-vacant model and (b) cis-vacant model. The pKa values of the trans-vacant clay model

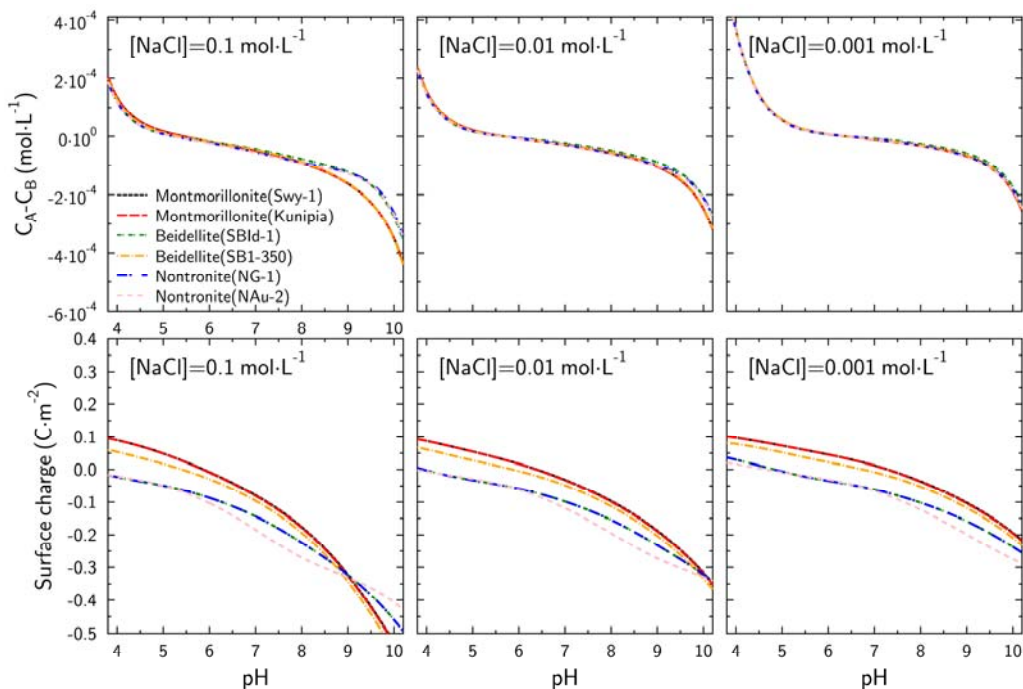592 were taken from Liu et al. (Liu et al. 2014a, 2015a)

593

28

594

595 **FIGURE 4.** Comparison of model predictions (lines) and potentiometric titration data (symbols)

596 for MX80 montmorillonite (bottom) and Swy-2 montmorillonite (top) as reported by Tournassat et

597 al (Tournassat et al. 2016).

598

599

600

FIGURE 5. Model predictions of potentiometric titration and surface charge curves for different 2:1 clay minerals. The modeled edge-specific surface area was set as 9 $m^2 \cdot g^{-1}$ and minor Fe^{3+} tetrahedral substitutions were considered to have the same pKa parameters as the Al^{3+} substitutions. All other parameters were consistent with those used by Gao et al. (2023).

605